Title
THERMODYNAMIC CONSIDERATIONS OF SOLID STATE SINTERING

Authors
Hoge, Carl E.
Pask, Joseph A.

Publication Date
1974-12-01

Submitted to Journal of the American Ceramic Society

LBL-3546
Preprint c. 1

THERMODYNAMIC CONSIDERATIONS OF SOLID STATE SINTERING

Carl E. Hoge and Joseph A. Pask

December, 1974

Prepared for the U. S. Atomic Energy Commission
under Contract W-7405-ENG-48

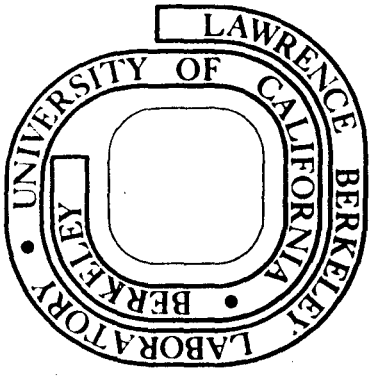

DISCLAIMER

THERMODYNAMIC CONSIDERATIONS OF SOLID STATE SINTERING

Carl E. Hoge and Joseph A. Pask

Inorganic Materials Research Division, Lawrence Berkeley Laboratory
and Department of Materials Science and Engineering,
College of Engineering; University of California,
Berkeley, California 94720

ABSTRACT

A theoretical analysis for solid phase sintering of idealized spherical particles packed in several ordered arrays was performed based on thermodynamic considerations. Results indicate that critical ratios of solid/solid over solid/vapor interfacial energies (γ_{ss}/γ_{sv}) represented by the dihedral angle, $\Phi_{critical}$, exist for any degree of densification of a sintering compact. If the equilibrium Φ_{eq} for a real material is greater than the $\Phi_{critical}$ determined at theoretical density for a specific idealized packing array, then no thermodynamic barrier to complete densification exists. However, if Φ_{eq} is less than $\Phi_{critical}$, endpoint densities will result. Additionally, a thermodynamic driving force exists for continued densification if the experimental or dynamic dihedral angle Φ_{dyn}, in a sintering compact is less than Φ_{eq}. This driving force may be expressed as $\Delta\Phi = \Phi_{eq} - \Phi_{dyn}$ and is dependent on corrosive, chemical and geometric effects. Experiments were performed to test the theoretical model using MgO compacts sintered under several different atmospheric conditions.

I. INTRODUCTION

If a packing of crystalline particles of equilibrium single phase composition is subjected to a sufficiently high temperature such that mass transport mechanisms become operative, the areas of solid/vapor interfaces decrease as solid/solid interfaces increase. This process is defined as sintering, and the basic driving force is the resulting reduction in free energy of the system. In order to fully characterize sintering, knowledge of thermodynamic as well as kinetic factors is thus necessary.

On sintering, particle/particle contacts or grain boundaries form and increase in area, and the compact normally shrinks by movement of material from the grain boundaries to free surfaces. The compact is characterized by a solid network and an interconnecting pore phase.[1] Upon further sintering, the pore phase generally becomes discontinuous and eventually is eliminated if it remains associated with grain boundaries. This point corresponds to the elimination of the solid/vapor interfacial area and the attainment of theoretical density. This point, however, does not constitute a minimum free energy configuration. Grain boundary migration and grain growth generally continue until planar grain boundaries[2-4] are attained. This process also goes on when the specimen is not theoretically dense.

The effect of thermodynamic factors on endpoint densities and densification rates in real compacts has as yet received little attention. Therefore, several idealized geometric packing models were studied theoretically in order to determine the thermodynamic constraints on densification. Some experimental data on the significance of geometric

configurations on sintering rates was also obtained.

II. THEORETICAL CONSIDERATIONS

(1) Thermodyanmics of Endpoint Densities

In a sintering powder compact the change in free energy of the system at constant temperature, pressure and phase composition can be expressed as

$$\delta(G_{syst}) = \delta \int \gamma_{sv} dA_{sv} + \delta \int \gamma_{ss} dA_{ss} \qquad (1)$$

where γ_{sv} = solid/vapor interfacial energy, γ_{ss} = solid/solid interfacial energy, dA_{sv} = decreasing differential solid/vapor interfacial area, and dA_{ss} = increasing differential solid/solid interfacial area. The first term on the right of the equation is always negative and the second, positive. Sintering will continue as long as the first term dominates, or $\delta(G_{syst})$ remains negative.

Four sintering geometries based on spherical particles of a uniform size were analyzed: diamond cubic (DC), simple cubic (SC), body-centered cubic (BCC), and face-centered cubic (FCC) (corresponding to particle coordination numbers of 4, 6, 8, and 12). The particles are assumed to be single phase, single crystals and to have isotropic interfacial energies. The interfacial energies are related to the dihedral angle by

$$\gamma_{ss} = 2\gamma_{sv} \cos \frac{\Phi}{2} \qquad (2)$$

The densification model used is based on the concept that the cap material removed at every contact, or grain boundary, between spheres is

uniformly distributed on the free surfaces. As the particle centers then move toward each other, the radii of the spheres increase in order to keep the total solid volume constant.[5] During this process, the dihedral angle increases. This model differs from that normally employed for predicting kinetics of solid phase sintering in which the material removed at a contact forms a bridging neck of increasing diameter. Although in most cases neck formation is experimentally observed during sintering and is associated with a decrease in free energy, such a geometry does not correspond to the minimum free energy configuration for the system and is thus an intermediate stage favored by kinetic considerations.

To illustrate: when two spheres are just in contact, Fig. 1A, the experimental Φ is zero. Now, if the spheres interpenetrate until a certain cap height, h_o, is removed and deposited in the neck region, Fig. 1B, the radius of each sphere is unchanged. At this point, if no further densification or change in h_o occurs but the solid/solid and solid/vapor interfaces equilibrate as shown in Fig. 1C, material from the neck region is deposited uniformly on the surfaces of the spheres causing R_o to increase to R and h_o to h_1 so that $R_o - h_o = R - h_1$, and Φ to assume the characteristic value for the configuration. The latter geometry, which corresponds to the minimum free energy configuration for that particular degree of densification, becomes the model used in this analysis. It becomes the equilibrium geometry when δG in Eq. (1) is numerically equal to zero. The critical values of γ_{ss}/γ_{sv} and the corresponding Φ can then be determined for this equilibrium configuration for any degree of shrinkage.

In a given packing if n_1 is the coordination of nearest neighbors around each sphere and P_1 is set as a variable equal to h_1/R (similar nomenclature to White and Stevenson,[5]) the solid/vapor and solid/solid interfacial areas for a sphere are given by

$$A_{sv} = 4\pi R^2 - 2\pi R h_1 n_1 = \pi R^2(4 - 2n_1P_1) \tag{3}$$

$$A_{ss} = \pi n_1 h_1(2R - h_1)/2 = \pi n_1 h_1 R(2 - P_1)/2 \tag{4}$$

If these values are substituted in Eq. (1) and $\delta(G_{syst})$ is set to zero, it becomes possible to determine the relationship* between γ_{ss}/γ_{sv} and P_1:

$$\frac{\gamma_{ss}}{\gamma_{sv}} = \frac{-2(4-3n_1P_1^2 + n_1P_1^3)^{2/3}\,(-2n_1) - \frac{2}{3}\,(4-3n_1P_1^2 + n_1P_1^3)^{-1/3}}{(4-3n_1P_1^2 + n_1P_1^3)^{2/3}\,(n_1(2-2P_1)) - \frac{2}{3}\,(4-5n_1P_1^2 + n_1P_1^3)^{-1/3}}$$

$$\frac{(-6n_1P_1 + 3n_1P_1^2)(4-2n_1P_1)}{(-6n_1P_1 + 3n_1P_1^2)(2P_1-P_1^2)n_1} \tag{5}$$

However, since densification is measured as $\Delta L/L_o$ (where L_o in this case is the original radius of the sphere) which is equivalent to h_o/R_o, P_1 or h_1/R can be recalculated as h_o/R_o or P_o. Critical values of γ_{ss}/γ_{sv}

*Detailed mathematical analyses are presented in the Ph.D. thesis of Carl Hoge, which is available as report LBL-3116.

can then be plotted as a function of h_o/R_o. Figure 2 shows curves for uniform size spherical particles in DC, SC, BCC and FCC packings. This plot is based on the minimum free energy densification model which corresponds to a starting value of 2 for γ_{ss}/γ_{sv} (0° dihedral angle) and a decrease of γ_{ss}/γ_{sv} (increase of dihedral angle) as shrinkage or h_o/R_o increases. The increasing dispersion of the curves with decrease of γ_{ss}/γ_{sv} is due to the fact that R increases more rapidly than h_1 as densification proceeds when the coordination number n_1 of nearest neighbors increases.

The interpenetration of spheres or shrinkage is represented by Eq. (5) in terms of P_1 for all packing arrays, regular or irregular, expressed by n_1 until second nearest neighbors touch or until a planar face in the unit cell has densified. This interval is represented by the a-b segments of each of the curves in Fig. 2. Each of the packing arrays then continues to sinter differently.

(A) SC Packing. For SC packing with a fractional void volume of 0.48, Fig. 3A, six nearest neighbors interpenetrate according to Eq. (5) and the densification is represented by segment a-b" of Fig. 2 until contacts form with second nearest neighbors along <110> directions, Fig. 3B. At this point, $P_0 = 0.184$, $\Phi_1 = 89.6°$, $\gamma_{ss}/\gamma_{sv} = 1.416$, fractional void volume = 0.036, and the (100) faces become completely densified. However, closed porosity remains along the (110) faces, Fig. 3B. With further densification interpenetration along primary contacts must continue resulting in reduction in the area of the (100) faces and in increase of Φ_1 beyond 90° along the (110) planes; also the second neighbor interpenetrations begin from $\Phi_2 = 0°$ (Fig. 3C). Just prior to complete

densification of the (110) face, the nearest neighbor dihedral angle (determined by graphical techniques) $\Phi_1 = 109°$, and $\gamma_{ss}/\gamma_{sv} = 1.161$. The second nearest neighbor dihedral angle $\Phi_2 = 89.6°$. The calculated value of P_o^1 at theoretical density is 0.196. Thus, no thermodynamic barriers exist for densification of a simple cubic array of spheres if equilibrium Φ_1 is greater than 109° or γ_{ss}/γ_{sv} for the system is less than 1.161. Kinetic barriers, however, may exist beyond $\Phi_1 = 89.6°$. Also, the 90° dihedral angles on the (100) faces at point b" constitute an unstable condition that could lead to further complexity by grain growth by demand of equilibrium 120° angles at triple points.

(B) BCC Packing. For BCC packing with a fractional void volume of 0.32, densification proceeds according to the model until contacts form with second nearest neighbors along <100> directions when the coordination of the spheres increases from 8 to 14. At this point h_o/R_o or P_o equals 0.102, fractional void volume is 0.062, and γ_{ss}/γ_{sv} is 1.734 or Φ_1 is 59.6°. With continued shrinkage, P_o and the nearest neighbor Φ_1 continue to increase, but the new contacts result in removal of cap material of height h_2 and the creation of second nearest neighbor Φ_2 which will always be smaller than Φ_1. The interpenetration continues until complete densification of the unit cell is realized. Equation (5) applies up to the point of second neighbor contacts (segment a-b in Fig. 2) and then has to be modified to take into account the contribution to the densification by the second neighbor contacts. At the point just prior to complete densification of the unit cell, the critical or nearest neighbor Φ_1 determined by graphical methods is 71.5° for which $\gamma_{ss}/\gamma_{sv} = 1.625$ (point c, Fig. 2) while the second nearest neighbor $\Phi_2 = 42°$ or

$\gamma_{ss}/\gamma_{sv} = 1.814$. The value of $\Delta L/L_o$, called P'_o in Table I, of 0.121 at theoretical density is calculated from the starting volume of the unit cell. The densification path from b to c in Fig. 2 is shown as a continuous line since open porosity is maintained to the end of densification for this packing. Thus, no thermodynamic barrier to the densification of a BCC array of spheres exists if the real value of γ_{ss}/γ_{sv} for the system is less than 1.625. At complete densification the solid/solid/vapor dihedral angle becomes a triple point with grain boundaries forming angles of 109°, 125.5°, and 125.5°. This configuration creates a driving force for grain boundary movement since the equilibrium angles are 120°, which would result in grain growth.

(C) DC Packing. For DC packing with a fractional void volume of 0.68, four nearest neighbors interpenetrate until contacts form with second nearest neighbors. Experimental γ_{ss}/γ_{sv} as a function of P_o is represented by Eq. (5) and by segment a-b' in Fig. 2. At b', $P_o = 0.277$, $\gamma_{ss}/\gamma_{sv} = 1.226$, $\Phi_1 = 104.4°$, and fractional void volume is 0.101 (Table I). With continued shrinkage, a modification of Eq. (5) can be achieved* as in the case for BCC packing since open porosity is maintained and is represented by segment b'-c' in Fig. 2. At point c', P_o is 0.280, $\gamma_{ss}/\gamma_{sv} = 1.074$, $\Phi_1 = 115°$, and a residual fractional closed porosity of 0.088 still remains. Based on a cube of unit edge length and 0.68 porosity theoretical density occurs at $P_o^1 = 0.316$. Because of the complex geometry the critical value of γ_{ss}/γ_{sv} at this point was not determined but it certainly would be expected to be less than 1.074.

---

*Detailed mathematical analyses are presented in the Ph.D. thesis of Carl Hoge, which is available as report LBL-3116.

(D) FCC Packing. For FCC packing with a fractional void volume of 0.26, 12 nearest neighbor spheres interpenetrate until the (111) face of the unit cell has densified completely, as represented by segment a-b"' of Fig. 2 and Eq. (5). Just before b"', $P_o = 0.084$, the solid vapor $\Phi_1 = 59.60$, experimental $\gamma_{ss}/\gamma_{sv} = 1.734$, and fractional closed pore volume = 0.035. When the (111) plane has densified at b"', a triple point with grains intersecting at 120° angles and a hexagonal network of grain boundaries form along this plane. With continued densification material must be removed from the (111) planes until contacts form with second nearest neighbors along (100) faces. At this point Φ_1 on the (100) plane is 90° and the plane is densified. Further shrinkage requires removal of material from the (111) and (100) planes and continued interpenetration on the (110) planes with Φ_1 increasing beyond 90° and Φ_2 increasing from 0°. At complete densification graphical methods indicate that $\Phi_1 = 109°$ and $\Phi_2 = 68°$, and calculated $P_o^1 = 0.095$. Therefore, if Φ_1 is greater than 109°, or the equilibrium γ_{ss}/γ_{sv} is less than 1.161, there is no thermodynamic barrier to complete densification of an FCC array of spheres.

(E) General. Analysis of the four sintering geometries indicates that the densification pattern is the same for any kind of uniform packing, regular or irregular, of uniform size spheres until second neighbor contacts are made or until densification is reached along some crystallographic plane. This stage is represented by Eq. (5) and the a-b segments in Fig. 2. In cases where second neighbor contacts are made, densification should proceed readily until complete densification is achieved along some plane or planes. This stage would be represented by expanding

Eq. (5) to take into account interpenetration along second neighbor contacts. A further mathematical modification is required when interaction begins to occur between interpenetrations or growing grain boundaries. In any case, no thermodynamic barriers to densification exist if the true or chemical γ_{ss}/γ_{sv} ratio for the system is smaller than the critical value for a particular packing. If densification is reached along some plane, however, closed pores form and further densification requires lateral transport of material from these planes; this condition could lead to kinetic barriers and grain boundary motion.

The BCC packing, however, is unique in that sintering continues after second neighbor contacts are made until complete densification is reached without the formation of any closed pores because each grain forms a 14-sided polygonal solid (tetrakaidecahedron) which fills space.

(2) Thermodynamic Driving Force

At any instance during sintering, if the experimental or dynamic dihedral angle is less than the equilibrium value determined by γ_{ss}/γ_{sv} for the system, a thermodynamic driving force exists for continued mass transport from the grain boundary to the adjoining free surfaces. The further the experimental dihedral angle is from the equilibrium value, the more negative is the differential free energy between the non-equilibrium and equilibrium configurations. The overall driving force for sintering may thus be expressed as

$$\Delta\Phi = \Phi_{eq} - \Phi_{dyn} \qquad (6)$$

where Φ_{eq} is the value based on γ_{ss} for a planar grain boundary and on γ_{sv} for surfaces in equilibrium with their own vapor; and Φ_{dyn} is the instantaneous value in a sintering compact which is dependent on geometry, chemical effects, and atmospheric conditions. When Φ_{dyn} becomes equal to Φ_{eq}, sintering ceases with an endpoint density unless Φ_{crit} for the packing is smaller than Φ_{eq} in which case there is no thermodynamic barrier for sintering.

Geometric changes also play a role in chemically stable systems in which bridging necks form between particles. Nichols[6] has shown mathematically that in the initial stage of sintering of two sphere models (actually infinite cylinders) bridging necks can form by "undercutting" the region adjacent to the neck by surface diffusion alone. Similar undercutting has also been predicted when volume diffusion mechanisms are operative.[7] These derivations assumed no contribution from the grain boundary energy to the shape of the surfaces, i.e., a 180° solid/vapor dihedral angle. The reverse surface curvature introduced by this neck formation is a thermodynamically unstable condition. A movement of material from the surface of the neck in the grain boundary region to the undercut region reduces or flattens out the degree of undercutting and in turn reduces the experimental dihedral angle. When Φ_{dyn} becomes smaller than Φ_{eq}, a thermodynamic driving force $\Delta\Phi$ exists for transport of material via bulk or grain boundary diffusion mechanisms from the grain boundary towards the dihedral angle region in order to restore the equilibrium dihedral angle. When these fluxes are similar to the surface diffusion fluxes, the two processes will continue on an atomistic scale until surface inflection points disappear and the equilibrium

configuration is reached. In this case $\Delta\Phi$ remains small throughout sintering in comparison with the presented sintering model wherein $\Delta\Phi$ is large at the beginning and decreases as the equilibrium configuration is approached, which is realized when the flux from the grain boundary is rapid compared to the surface diffusion flux.

If the surface diffusion flux is rapid compared to the bulk or grain boundary diffusion flux, movement of material from the free surfaces tends to form necks without undercutting and thus maintain Φ_{eq} without any measurable densification.

Chemical effects, such as adsorption or desorption of material at surfaces and interfaces from the bulk or vapor will affect the surface and interfacial energies and thus Φ.

Atmospheric conditions become a factor in sintering if they cause nonequilibrium between the solid and vapor. If vaporization is rapid compared to other mass transport mechanisms which attempt to realize an equilibrium dihedral angle, a non-equilibrium or experimental Φ_{dyn} which is smaller than Φ_{eq} will be maintained until closed pores are formed. This decrease in Φ_{dyn} and corresponding increase in $\Delta\Phi$ can be referred to as a "corrosion" effect. When closed porosity forms, the internal dihedral angles will change toward Φ_{eq} under a static or equilibrium vapor either with or without additional sintering depending upon the value of Φ_{crit}. However, if a back pressure is built up within the pore, the pore along a grain boundary or triple point will assume the minimum free energy configuration with equilibrium dihedral angles.

III. EXPERIMENTAL PROCEDURES

An experimental verification of the thermodynamic predictions could consist of choosing several single phase isotropic materials identical in every way except with different γ_{ss}/γ_{sv} or Φ_{eq} values, cold pressing them to the same green density, and sintering them under identical conditions. If the Φ_{crit} for a given packing in each case was larger than Φ_{eq}, the material with the largest Φ_{eq} should have the highest endpoint density. On the other hand, if Φ_{eq} in each case was larger than Φ_{crit}, all the materials would reach theoretical density from a thermodynamic viewpoint but at different rates. It is, however, practically impossible to realize such experimental conditions.

An experimental verification of thermodynamic predictions was made by an analysis of MgO compacts sintered at 1510°C under different atmospheric conditions. If the gases in the atmosphere affect γ_{sv} and/or γ_{ss}, or create corrosive effects, the experimental dihedral angles will vary. These differences can then be correlated to the densities and/or rates of densification of the sintering powder compacts.

(1) Preparation of Powder Compacts

MgO powder was prepared by calcining Mallinckrodt $MgCO_3$ at 1000°C in a heavy duty type furnace for 24 h in air and furnace-cooled. The powder was then ground in an alumina mortar with pestle to break up the calcined cake. After grinding, it was dispersed in ethyl alcohol and immediately dried at 110°C. Compacts, 1.77 cm dia. and ∿1 cm thick, were formed by cold pressing in a steel die using no binders to a green density of 45% of theoretical. Fifteen compacts were prepared for each sintering run.

(2) Sintering and Density Measurements

Sintering anneals were made with three different atmospheric conditions: static air, flowing air, and flowing water vapor. In each case the specimens were arranged on a porous ceramic pedestal that was raised into the furnace which was maintained at a temperature of 1200°C. The temperature was then raised to 1510°C in 30 min and held for 100, 700, 1440, and 2880 min. After annealing, the specimens were cooled to 1200°C and removed from the furnace.

The static air experiments were made with no gaseous introductions. For the series with flowing air, compressed air was passed into the furnace by means of a tube running along the axis of the pedestal permitting the air to flow directly over the specimens. A similar setup was used for the flowing water vapor atmosphere. Distilled water was boiled in a sealed vessel and carried through heated glass tubing directly into the furnace. The flow rate for both cases was approximately 2.0 cu. ft/h and maintained during the cooling step.

After each sintering run the bulk density was determined for each specimen using the displacement technique in distilled water. The standard deviation and variance were calculated for the distribution of 15, and for a reduced distribution of 13 specimens after the specimens with the largest positive and negative deviation were eliminated. Fracture surfaces of selected specimens were also prepared for SEM examination.

(3) Dihedral Angle Measurements

Direct measurements of the dihedral angles of sintered specimens could not be performed since the densities of the sintered compacts were

less than 90% of theoretical, and the grain sizes were too small. In order to approximate sintering conditions, specimens for dihedral angle measurements were hot pressed from similarly prepared MgO powder in a graphite die at 1200°C for 30 min in a vacuum of 5×10^{-4} torr to a density of 98.5% of theoretical. After hot pressing, the specimens were annealed at 1700°C for 1440 min (24 h) in order to realize sufficient grain growth for dihedral angle measurements. The grain size was approximately 100 microns.

The annealed polycrystalline material was cut into 0.5 cm cubes and one surface of each cube was polished on a succession of diamond wheels and cloths to a finish of 0.25 microns. A final polish with Linde B alumina was performed just prior to experimentation. A polished specimen was then annealed for 1440 minutes at 1510°C under a number of atmospheric conditions. Twenty-four hours was chosen as an annealing time since it allowed sufficient diffusion so that grain boundaries intersecting the polished surface were thermally grooved to a width and a depth to permit measurement of the dihedral angles which was performed according to the method of Achutaramayya and Scott.[8] The technique consisted of orienting the surface of the specimen perpendicular to the beam of the SEM. A contamination line of carbon was deposited perpendicular to the grain boundary groove. The specimen was then tilted 47° around the axis of the contamination line, and the profile of the groove was photographed.

The dihedral angle, Φ, was calculated from the measured groove angles θ_1 and θ_2 according to Eqs. (7), (8), and (9).

$$\text{Tan } \alpha_1 = \text{Sin (Tilt Angle) Tan } \theta_1 \quad (7)$$

$$\text{Tan } \alpha_2 = \text{Sin (Tilt Angle) Tan } \theta_2 \quad (8)$$

$$\Phi = \alpha_1 + \alpha_2 \quad (9)$$

Since θ_1 and θ_2 are measured separately, the true dihedral angle is obtained even if the grain boundary is not perpendicular to the surface of the specimen.

IV. RESULTS AND DISCUSSION

(1) Sintering

Density values of sintered specimens which were annealed at 1510°C for varying times in several atmospheres are given in Table II and are plotted in Fig. 4 as density versus time. A considerably faster densification rate was observed in flowing water vapor. Similar results have been reported by others.[9-12]

Slower sintering rates were observed in flowing air and static air atmospheres but if the time at temperature was extended sufficiently, all sintered specimens approached the same endpoint density. Specimens sintered in water vapor realized their principal densification within the first 100 min and reached maximum density (3.3 g/cc) at 700 min. In flowing air, specimens reached maximum density at about 1440 min; and in static air, at more than 2880 min. This density corresponds to about 93% of theoretical which was considered to be at least partially due to nonhomogeneity in the unfired compact.

Fracture surfaces of specimens sintered in flowing water vapor indicated no significant grain growth during the first 100 min, but approximately a five fold increase in grain size occurred between 100 and 1440 min. Fracture surfaces of specimens sintered in static air and flowing air for 1440 min indicated similar grain sizes which were about the same size as the grain size of specimens sintered in flowing water vapor for 700 min.

It should be noted that as the grain size of the specimens sintered in flowing water vapor from 100 to 1440 min increased, the size of the pores on the grain boundaries also increased, as would be expected since the densities remained essentially the same. Since the fractures were essentially transgranular, pores were also revealed on the cleavage planes that were not associated with grain boundaries; these pores are expected to be associated with nonhomogeneity in the green compact and grain boundary motion. It is a well established experimental fact that as the volume fraction of inclusions or porosity decreases, the mobility of grain boundaries increases.[4,13,14] Therefore, the larger grain size of the compacts sintered in flowing water vapor as compared to flowing air or static air can be attributed to the faster initial densification rate of the former.

(2) Dihedral Angles

Table III lists the dihedral angle measurements of grain boundary grooves of hot-pressed polycrystalline MgO annealed in atmospheres of static air (96°), flowing air (56°), flowing water vapor (32°), and flowing water vapor followed by static air (96°). Figure 5 (2000X) shows a surface of a hot-pressed specimen of MgO which was annealed in

static air, and Fig. 6 (20,000X) shows a grain boundary groove of this specimen tilted relative to the axis of the contamination line (dark line) permitting measurement of the dihedral angle. This experiment would be expected to most closely approach equilibrium conditions since it is most likely to be in equilibrium with its own vapor, and exhibits the largest dihedral angle.

The specimen sintered in flowing air has a dihedral angle of 56°. Since the groove root of a grain boundary intersecting a surface has a positive curvature and a stress concentration exists in the grain boundary at the root, a higher vapor pressure exists above the groove root than above a planar surface. Under dynamic conditions, the vapor species above a specimen can be swept away. As the system attempts to restore the equilibrium vapor pressure, material vaporizes more from the higher energy curved surface at the groove root. If vaporization is rapid compared to other mass transport mechanisms which attempt to restore the equilibrium shape of the dihedral angle, a nonequilibrium or experimental dihedral angle which is smaller than the equilibrium angle will result.

The smallest experimental dihedral angle (32°) was observed for a specimen annealed in flowing water vapor. It is not known what effect water vapor may have on the interfacial energies of MgO at 1510°C. It has been reported that negligible water vapor exists on the surface at 1000°C[15-17] and that in the presence of static water vapor a transient molecular adsorption or chemisorption of water vapor on MgO may occur with a reduction of γ_{sv}.[18] If the grain boundary energy is unaffected, then the dihedral angle would be reduced over that in static air as observed. A more likely explanation under flowing conditions, however,

is that a molecular layer of adsorbed hydroxide does not form but a complex of H_2O and MgO can form which has a higher vapor pressure than MgO gas.[11] This reaction would occur more readily at the groove root because of a higher stress concentration. Vaporization of a complex is supported by the appearance of precipitates on the surface of the specimen, as shown in Fig. 7 (2000X), which probably formed on cooling from the test temperature. This condition would then result in a corrosion effect with a smaller nonequilibrium or dynamic dihedral angle since γ_{sv} would be expected to remain the same as that for the static air value.

Another experiment was performed to determine the effect on the dihedral angle if nonequilibrium conditions were introduced and then essentially removed. A specimen was annealed for the first 700 min in flowing water vapor and then for an additional 700 min in static air. The measured dihedral angle was 96° which is identical to the static air value.

(3) Correlation of Densification with Driving Forces for Sintering

At any instance during sintering, if the experimental or dynamic dihedral angle is less than the equilibrium value, there is a thermodynamic driving force expressed as $\Delta\Phi$ for continued mass transport from the grain boundary to the adjoining surfaces and sintering. The value of Φ measured in static air was used as the equilibrium dihedral angle. The differences, $\Delta\Phi_{corr}$ between the dihedral angles in static air and other atmospheres given in Table III represent the driving force due to the corrosion effect alone. Figure 4 indicates that the larger is the value of $\Delta\Phi_{corr}$, the greater is the density at any given time. The growth of grains and pores with essentially no increase in density during

the sintering of compacts in H_2O vapor beyond 100 minutes of sintering suggests the loss of the corrosion effect due to the formation of closed pores.

For MgO compacts used in this study, the maximum measured value of 96° for Φ was considered to be Φ_{eq}. Although the particle packing was irregular and inhomogeneous, the average bulk green void volume of 0.55 was similar to that for simple cubic packing which has a value of Φ_{crit} of 90° when second nearest neighbors touch to form closed pores, and of 109° for complete densification. Therefore, no thermodynamic barrier would be expected for densification up to the point where second nearest neighbors touch, but there may be one to reach complete densification resulting in an endpoint density.

The slow densification rate for the sintering experiments in static air suggests that "necks" formed at particle-particle contacts resulting in Φ_{eq}. The driving force then is due to an upset of Φ from equilibrium because of mass transport due to the reverse curvatures of the particle surfaces in the neck regions attempting to reach a minimum energy configuration. Under these conditions, $\Delta\Phi$ remains small. In flowing atmospheres, however, the corrosion effect tends to decrease Φ_{dyn} and increase $\Delta\Phi$ with an increase of the sintering rates above those for static air.

V. CONCLUSIONS AND SUMMARY

(1) Theoretical Consideration

The thermodynamic analysis of solid state sintering indicates that a small γ_{ss}/γ_{sv} ratio for the system and a high density of the unfired compact favor densification, and also that the ratio must be less than the

critical ratio for a given packing of particles to reach theoretical density. Therefore, any additives that would reduce γ_{ss} relative to γ_{sv} would enhance sintering, or make sintering densification possible if the γ_{ss}/γ_{sv} ratio for a given material is then reduced below the critical value.

Additionally, the thermodynamic driving force for sintering, $\Delta\Phi$, is given by Eq. (6) and is dependent on geometry, chemical effects, and corrosion. Corrosion is effective during the open pore stage of sintering.

The model presented here is based on uniform packing of spheres of a given size with isotropic interfacial energies. Sintering of such systems would not lead to grain boundary motion or grain growth in the open pore stage although motion would probably occur after development of second neighbor contacts due to geometric formation of nonequilibrium triple point configurations. In real systems complexities are introduced because of a range of particle sizes and shapes, anisotropy of interfacial energies and non-uniformity of packing. Only the latter factor has been discussed. The other factors could develop conditions favorable for grain boundary motion and grain growth during the open pore stage. These factors are presently being considered. This discussion, however, should provide an initial contribution to the understanding of the factors that are critical in controlling the sintering process.

(2) Experimental Considerations

Sintering studies of MgO compacts annealed in three different atmospheres at 1510°C revealed that the fastest sintering rate occurs in flowing water vapor and the slowest in static air. All specimens yielded

approximately the same endpoint density of 93% of theoretical although they attained this density at different sintering rates.

Corresponding dihedral angle measurements indicated that the smallest value (32°) occurred in flowing water vapor and the largest in static air (96°). The corrosive effect of a flowing water vapor atmosphere leads to a small Φ_{dyn} and a large $\Delta\Phi$ which is maintained during sintering and thus prevents neck formation between particles. In static air, no corrosive effects occur; a bridging neck probably forms between particles reducing $\Delta\Phi$ and thus also the sintering rate.

It is not known whether the 93% theoretical density which was attained is a true endpoint density or was due primarily to inhomogeneities introduced during fabrication of the compacts. For compacts with an unfired density of 45% theoretical, if 96° is the true equilibrium dihedral angle for MgO at the experimental temperature, the observed endpoint densities are not completely due to inhomogeneities but are also partially due to thermodynamic endpoint densities reached in certain regions of the packings.

ACKNOWLEDGMENT

This work was done under the auspices of the United States Atomic Energy Commission.

REFERENCES

1. V. A. Iversen, "Phenomenological Analysis of the Densification Kinetics of Metal Powders During Sintering IV. An Approximate Method of Evaluating the Parameters of an Arbitrary Beginning of Isothermal Densification," Soviet Powder Metallurgy and Metal Ceramics, Consultants Bureau, 1970, pp. 552-6.

2. R. L. Coble, "Effects of Particle-size Distribution in Initial-Stage Sintering," J. Am. Ceram. Soc. 56 (9) 461-6 (1973).

3. J. Vdovic, Eine neue Sintergleichung und Ihre Experimentelle Uberprufung, Planseeberichte fur Pulvermatallurgie, Bd. 19, 1971.

4. B. H. Alexander and R. W. Balluffi, "The Mechanism of Sintering of Copper," Acta Met. 5, 666-77 (1957).

5. I. M. Stephenson and J. White, "Factors Controlling Microstructure and Grain Growth in Two-Phase (One Solid + One Liquid) and Three-Phase (Two Solid + One Liquid) Systems," Trans. British Ceram. Soc. (1967).

6. F. A. Nichols, "Theory of Sintering of Wires by Surface Diffusion," Acta Met. 16 103-13 (1968).

7. K. E. Easterling and A. R. Tholen, "Computer Simulated Models of the Sintering of Metal Powders," Zeitschrift fur Mettalkunde, 1970.

8. G. Achutaramayya and W. D. Scott, "Measurement of Dihedral Angles by Scanning Electron Microscopy," J. Am. Ceram. Soc. 56 (4) 230-1 (1973).

9. P. F. Eastman and I. B. Cutler, "Effect of Water Vapor on Initial Sintering of Magnesia," J. Am. Ceram. Soc. 49 (10) 526-30 (1966).

10. P. J. Anderson and P. L. Morgan, "Effect of Water Vapour on Sintering of MgO," Trans. Faraday Soc., 60 (5) 930-7 (1964).

11. J. White, "Refractories Research II. Calcination and Sintering of Magnesia," J. Australian Ceram. Soc., 9 (2) 60-3 (1973).

12. G. H. Jonker and W. Noorlander, Science of Ceramics, "Grain Size of Sintering Barium Titanate," ed. Stewart, Vol. 1, 1962, pp. 255-64.

13. J. E. Burke, "Role of Grain Boundaries in Sintering," J. Am. Ceram. Soc. 40 (3) (1957).

14. L. Seigle, Kinetics of High Temperature Processes, "Role of Grain Boundaries in Sintering," Tech. Press M.I.T., and J. Wiley, London, 1959, ed. Kingery, pp. 172-8.

15. R. E. Razouk and R. Sh. Mikhail, "The Sorption of Water Vapor on Magnesium Oxide," J. Phys. Chem. 59 (7) 636-40 (1955).

16. P. J. Anderson, R. F. Horlock, and J. F. Oliver, "Interaction of Water with the Magnesium Oxide Surface," Trans. Faraday Soc., 61 (12) 2754-62 (1965).

17. A. F. Bessonov and V. M. Ust'yantsev, "Effect of the State of the Surface Layers on Particles on the Sintering of Magnesite Powders," Soviet Pwdr. Met. and Met. Cer. No. 5, 1965, pp. 365-7.

18. P. J. Anderson and P. L. Morgan, "Effect of Water Vapour on Sintering of MgO," Trans. Faraday Soc., 60 (50) 930-7 (1964).

Table I. Parameters for solid phase sintering models

	DC	SC	BCC	FCC
Fractional initial void volume:	0.68	0.48	0.32	0.26
At point of second neighbor contacts or endpoint of Eq. (5)				
P_0 (Linear shrinkage based on Eq. (5))	0.277	0.184	0.102	0.084
Φ_1 (dihedral angle)	104.4	89.6	59.6	59.6
γ_{ss}/γ_{sv}	1.226	1.416	1.734	1.734
Fractional void volume	0.101	0.036	0.062	0.035
At theoretical density:				
P_0' (Linear shrinkage of cube with original edge length of 1)	0.316	0.196	0.121	0.095
Φ_1 (dihedral angle)		109	71.5	109
γ_{ss}/γ_{sv}	<1.074	1.161	1.625	1.161

Table II. Densities under varying sintering conditions at 1510°C

Time in minutes	50	100	700	1440	2880
Static Air					
Density (13 specimens)	-	1.921	2.550	3.043	3.270
Std. Deviation	-	0.024	0.131	0.018	0.038
Flowing Air					
Density (13 specimens)	-	2.039	3.017	3.280	-
Std. Deviation	-	0.042	0.035	0.038	-
Flowing Water Vapor					
Density (13 specimens)	3.165	3.200	3.324	3.299	-
Std. Deviation	0.033	0.040	0.019	0.019	-

Table III. Dihedral angles under varying sintering conditions at 1510°C

Experimental Conditions	Dihedral Angle	γ_{ss}/γ_{sv}	$\Delta\Phi_{corr}$*
Static Air	96°	1.33	0.0°
Flowing Air	56°	1.81	40°
Flowing Water Vapor	32°	1.92	64°
Flowing Water Vapor followed by Static Air	96°	1.33	0.0°

*Driving force for sintering due to corrosion effect.

FIGURE CAPTIONS

Fig. 1. Interpenetration at two sphere contact and distribution of mass in neck region and in minimum free energy configuration.

Fig. 2. Fractional shrinkage vs critical γ_{ss}/γ_{sv} ratio for different arrays of uniform size spheres.

Fig. 3. Densification steps on sintering spheres in simple cubic packing: (a) at start, (b) complete densification on (100) face, and (c) continued densification along (110) face.

Fig. 4. Density vs time for MgO compacts sintered at 1500°C in several atmospheres.

Fig. 5. Surface of hot pressed MgO specimen annealed in static air (2000X).

Fig. 6. Grain boundary groove tilted 47° around the axis of the contamination line.

Fig. 7. Precipitates on the surface of a specimen annealed in flowing water vapor at 1510°C for 1440 minutes, which probably formed on cooling from the test temperature.

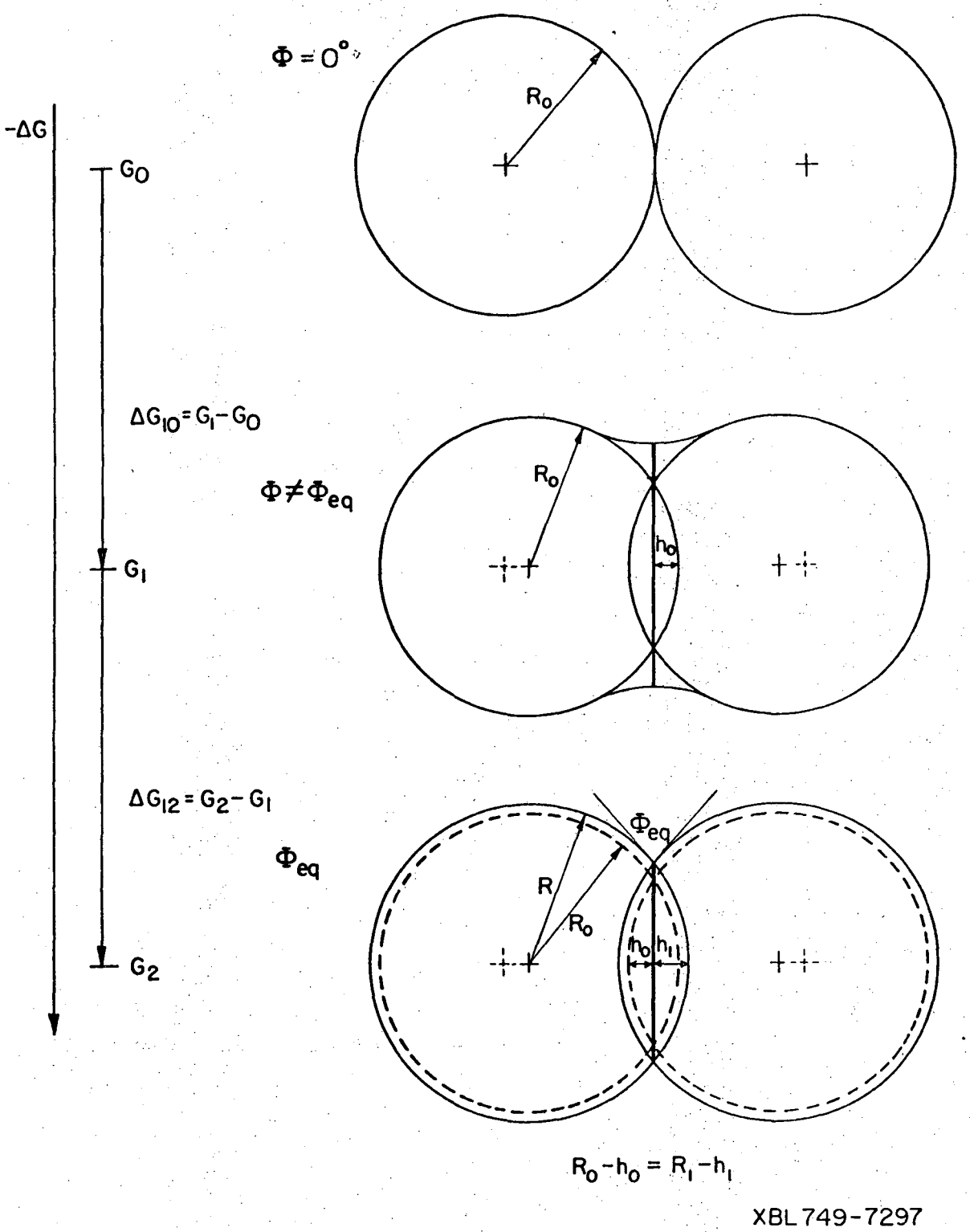
Φ = 0°
R_o
-ΔG
G_0
$\Delta G_{10} = G_1 - G_0$
$\Phi \neq \Phi_{eq}$
R_o
h_o
G_1
$\Delta G_{12} = G_2 - G_1$
Φ_{eq}
Φ_{eq}
R
R_o
h_o
h_1
G_2
$R_o - h_o = R_1 - h_1$
XBL749-7297

Fig. 1

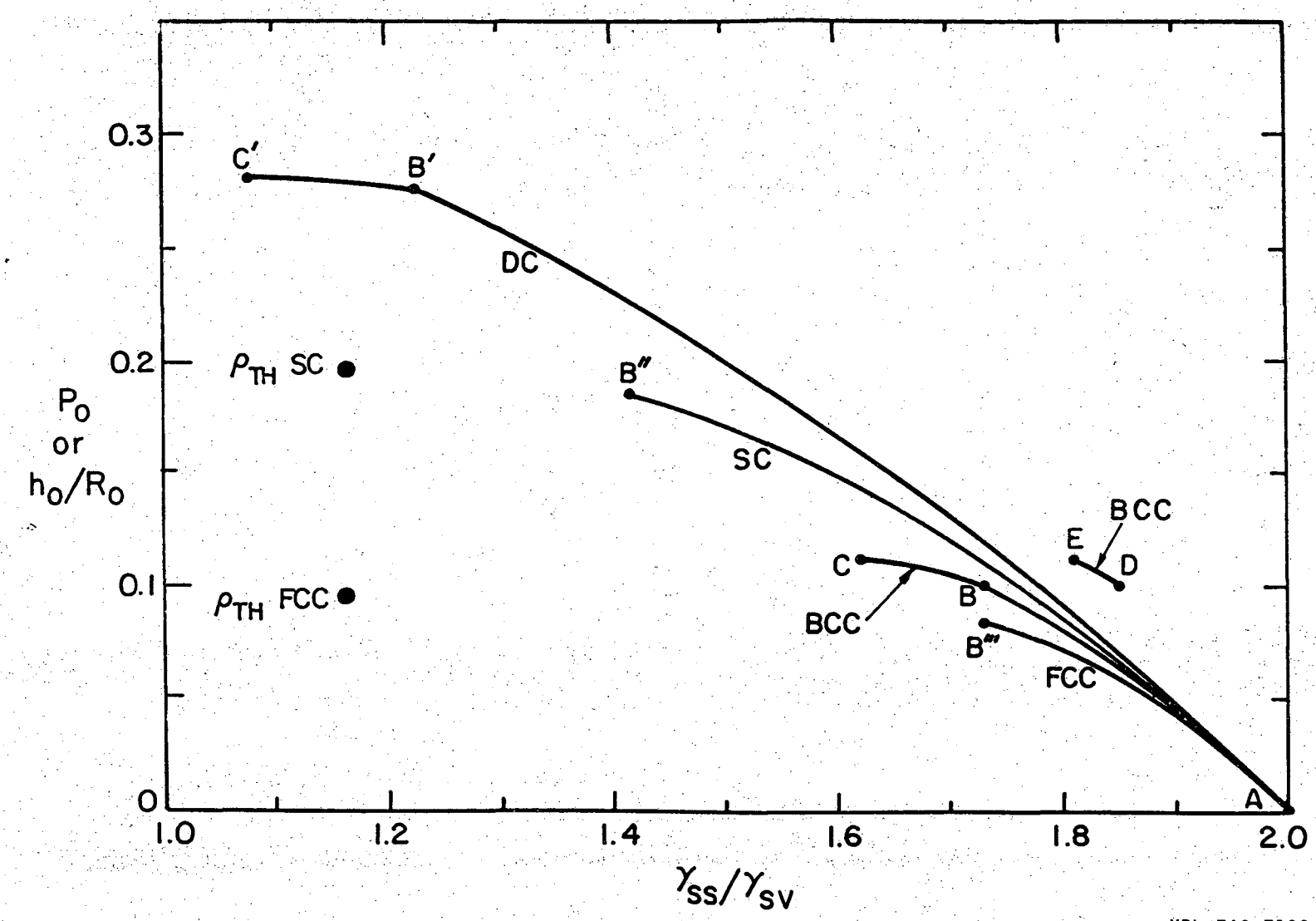

Fig. 2

XBL 749-7198

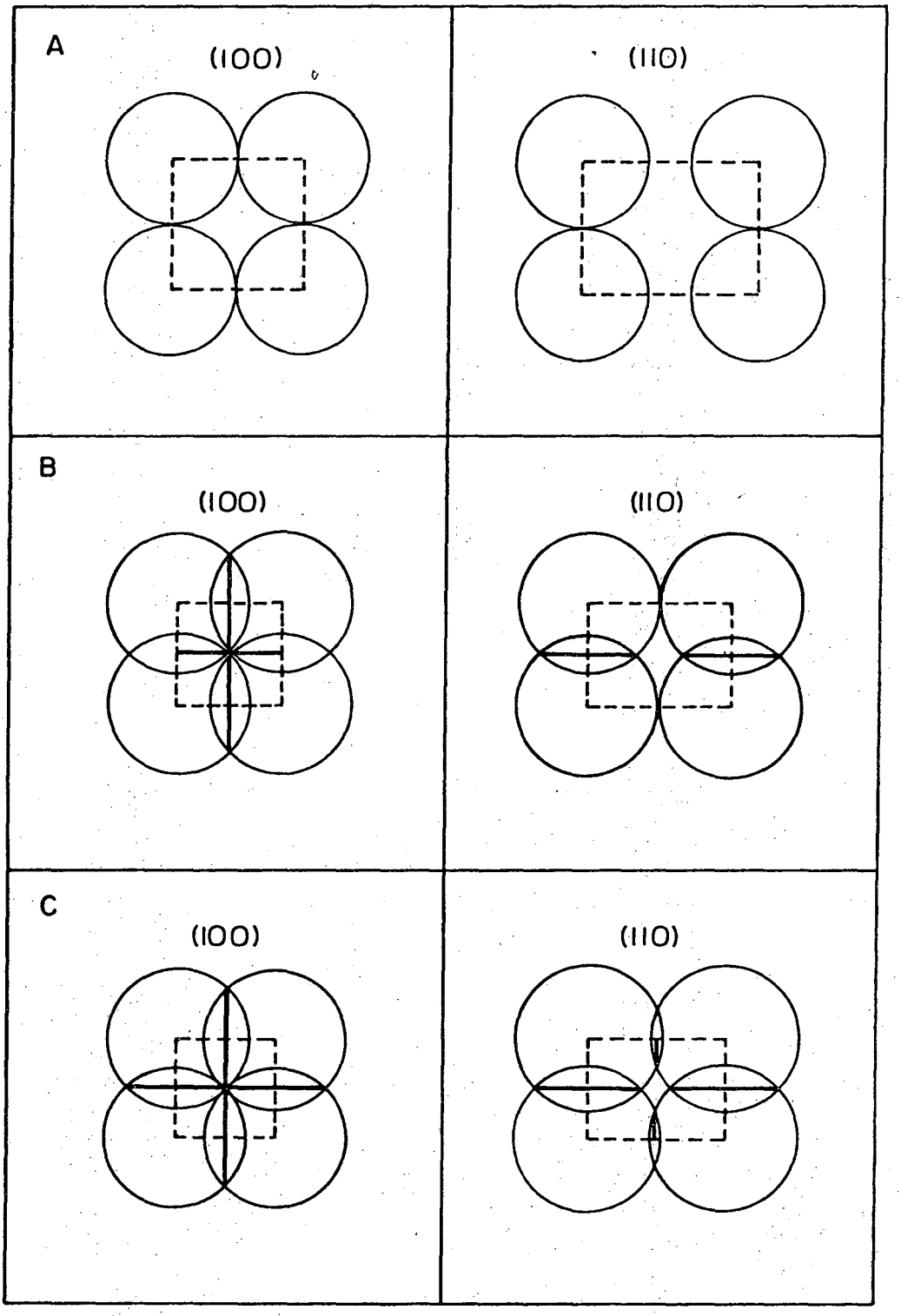

XBL 749-7293

Fig. 3

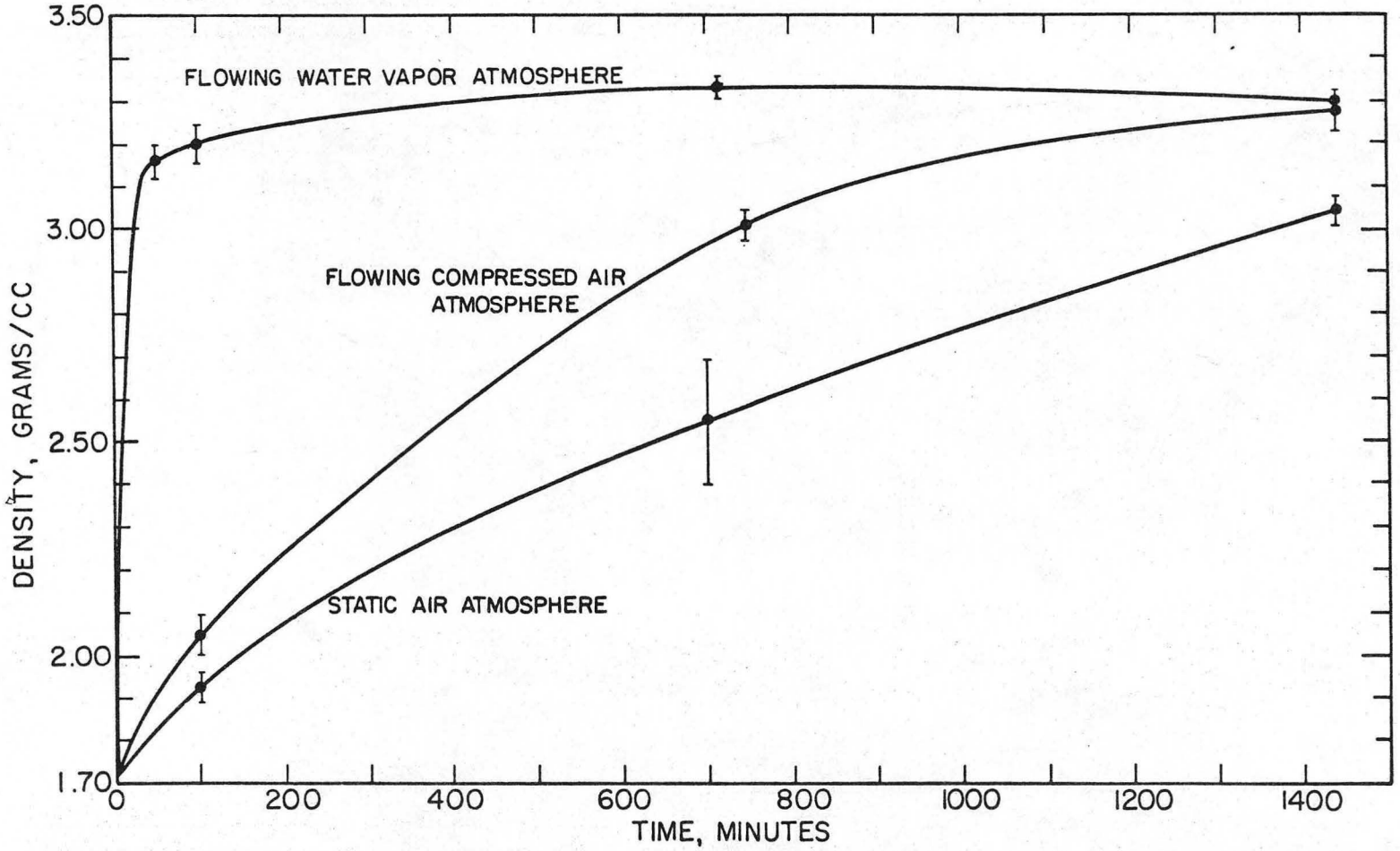

Fig. 4

XBL 749-7341

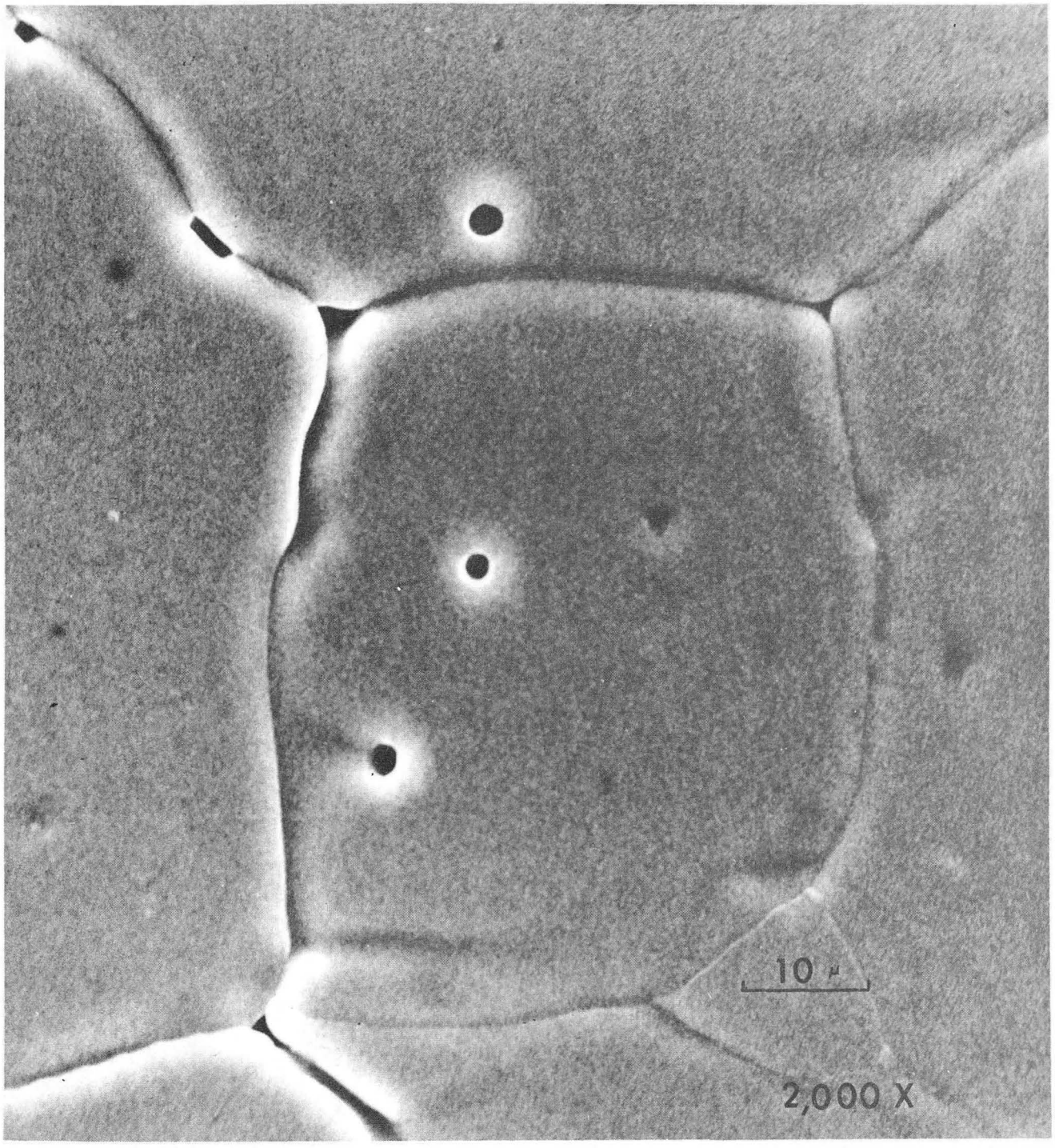

XBB 747-4568

Fig. 5

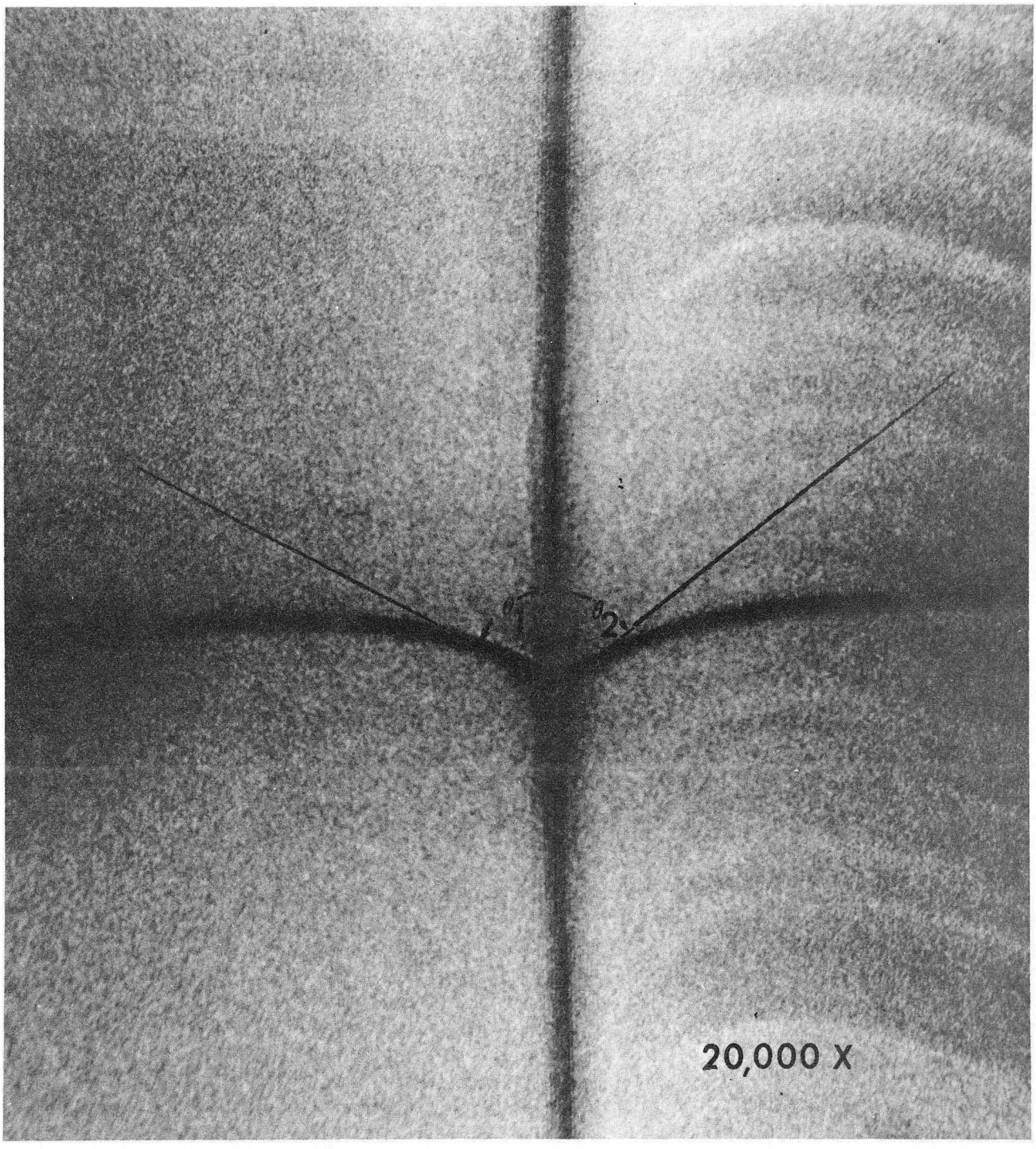

XBB 747-4558

Fig. 6

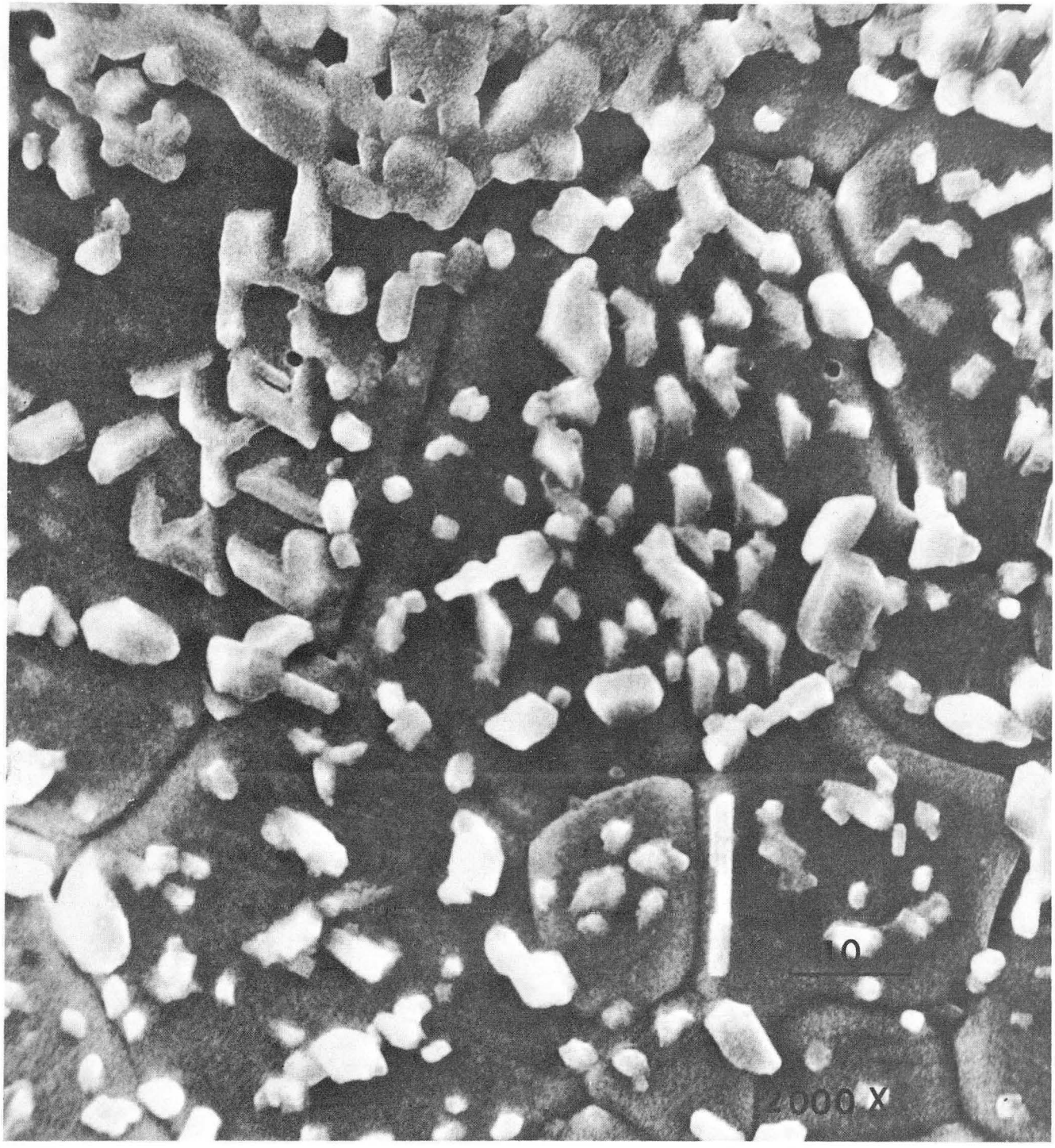

XBB 747-4562

Fig. 7

TECHNICAL INFORMATION DIVISION
LAWRENCE BERKELEY LABORATORY
UNIVERSITY OF CALIFORNIA
BERKELEY, CALIFORNIA 94720